ARL-TR-9890 ● MAR 2024

Toward the Use of Surrogate Post-Detonation Gas Mixtures to Study Aluminum Laser-Induced Plasma Chemistry

by Elliot R Wainwright, Nikolas Deo, and Jennifer L Gottfried

NOTICES

Disclaimers

The findings in this report are not to be construed as an official Department of the Army position unless so designated by other authorized documents.

Citation of manufacturer's or trade names does not constitute an official endorsement or approval of the use thereof.

Destroy this report when it is no longer needed. Do not return it to the originator.

ARL-TR-9890 ● MAR 2024

Toward the Use of Surrogate Post-Detonation Gas Mixtures to Study Aluminum Laser-Induced Plasma Chemistry

Elliot R Wainwright and Jennifer L Gottfried
DEVCOM Army Research Laboratory

Nikolas Deo
Department of Defense (DOD) Historically Black Colleges & Universities and Minority Serving Institutions (HBCU/MI) Summer Research Internship Program
University of California, Riverside

REPORT DOCUMENTATION PAGE

1. REPORT DATE	2. REPORT TYPE	3. DATES COVERED	
		START DATE	END DATE
March 2024	Technical Report	6/5/23	12/11/23

4. TITLE AND SUBTITLE
Toward the Use of Surrogate Post-Detonation Gas Mixtures to Study Aluminum Laser-Induced Plasma Chemistry

5a. CONTRACT NUMBER	5b. GRANT NUMBER	5c. PROGRAM ELEMENT NUMBER
5d. PROJECT NUMBER	**5e. TASK NUMBER**	**5f. WORK UNIT NUMBER**

6. AUTHOR(S)
Elliot R Wainwright, Nikolas Deo, and Jennifer L Gottfried

7. PERFORMING ORGANIZATION NAME(S) AND ADDRESS(ES)
DEVCOM Army Research Laboratory
ATTN: FCDD-RLA-WA
Aberdeen Proving Ground, MD 21005

8. PERFORMING ORGANIZATION REPORT NUMBER
ARL-TR-9890

9. SPONSORING/MONITORING AGENCY NAME(S) AND ADDRESS(ES)	10. SPONSOR/MONITOR'S ACRONYM(S)	11. SPONSOR/MONITOR'S REPORT NUMBER(S)

12. DISTRIBUTION/AVAILABILITY STATEMENT
DISTRIBUTION STATEMENT A. Approved for public release: distribution unlimited.

13. SUPPLEMENTARY NOTES
ORCIDs: Elliot R Wainwright, 0000-0002-2301-9420; Jennifer L Gottfried, 0000-0002-1282-1928

14. ABSTRACT
Metals under high-energy nanosecond laser excitation undergo ablation, phase explosion, entrainment, and subsequent reaction in the extreme environment of a laser-induced plasma where ionization levels, excitation temperatures, and instantaneous pressures are high. In this study, we illustrate the reactions of aluminum (Al) under different detonation-relevant atmospheric conditions. We control the environment within a small-scale vacuum chamber using dynamic gas mixing techniques and use mixtures representing equilibrium state gas compositions predicted by thermochemical code following the detonation of several common explosives. We probe the environmental effects using schlieren imaging to track the laser-induced shock wave and gated, high-resolution mid-to-near ultraviolet and visible spectroscopy at the hundreds of nanosecond to tens of microsecond timescale to track reaction species. Enhancement of plasma properties (e.g., electron density, ionization ratio) and stochastic behavior in the laser-induced shock velocity with the presence of argon is observed. A matrix of comparisons among plate and powder Al, detonation gas mixture content, and temporal evolution behaviors is broadly characterized and cataloged. These experiments help us understand the reactions of Al in anaerobic plasma environments generated from detonations in a microscale high-throughput way.

15. SUBJECT TERMS
anaerobic reaction; detonation gases; LASEM; LIBS; metal powders; reactive materials; Weapons Sciences

16. SECURITY CLASSIFICATION OF:			17. LIMITATION OF ABSTRACT	18. NUMBER OF PAGES
a. REPORT	b. ABSTRACT	C. THIS PAGE		
UNCLASSIFIED	UNCLASSIFIED	UNCLASSIFIED	UU	42

19a. NAME OF RESPONSIBLE PERSON	19b. PHONE NUMBER *(Include area code)*
Elliot R Wainwright	(44) 371-6717

STANDARD FORM 298 (REV. 5/2020)
Prescribed by ANSI Std. Z39.18

Contents

List of Figures

List of Tables

Acknowledgments

The authors thank Frank De Lucia Jr (ARL), and Wendy Beardsley and Burt Beardsley (Catalina Scientific Inc.) for their insightful discussions and diagnostic assistance.

1. Introduction

Materials subjected to focused nanosecond laser pulses experience extreme heating rates and instantaneous pressures, generate nano-particulates due to phase explosion, and subsequently react in the laser-induced plasma once the plasma begins to cool to favorable levels for recombination and condensation to occur. The resulting plasma is a highly dynamic mixture of ablated species, particle fragments, gaseous transients, condensing particles, oxidants, and so on, and it can exhibit significant deviations from local thermodynamic equilibrium (LTE).[1] The heating rate of these laser-induced plasmas can approach 10^{10} to 10^{13} K/s depending on the timescale, species, and methodology used to make the temperature measurement. For example, kinetic temperatures of atoms within the plasma often exceed thousands of degrees at 1 ms (higher at earlier timescales) and rapidly cool on the microsecond timescale; these temperatures are typically significantly lower than the calculated excitation temperatures.[2] Instantaneous pressures within the initial plasma kernel can reach tens of gigapascals.[3] These conditions are similar to detonation events, in which condensed phase components rapidly gasify behind a shock wave with similar temperatures, pressures, and ionized gases.[4–6]

Reactions of metals within laser-induced plasmas have received significant attention through laser-induced breakdown spectroscopy (LIBS) studies, including the oxidation of ablated gas-phase metal species following the laser-induced plasma.[7–12] Our recent studies have focused on morphological, microstructural, particle-size variations of powder materials under fixed laser conditions to understand plasma properties such as species evolution, plasma temperatures, electron densities, and hydrodynamics within the plasma.[13–16] Moreover, these studies have focused on trying to connect spectral properties with energy release as measured through laser-induced shock-wave measurements. A laser-induced shock wave, when little or no reactive material is present, is well represented by the Sedov–Taylor–Von Neumann representation in which the shock-wave evolution can be assumed from an instantaneous, massless point source of energy (e.g., the input laser energy).[17,18] Although valid at early times following the laser pulse (e.g., Mach numbers <5[19]), this assumption breaks down if there is a time and mass component to the energy release, because continued energy release in time will cause deviations in this classic shock to acoustic transition similar to that observed in chemical explosives.[20] This deviation is measured in the laser-induced air shock from energetic materials (LASEM) method, in which laser-induced shock-wave measurements between energetic samples (either radius or Mach number) can be used as a surrogate energy release metric at times relevant to the shock expansion through the plasma (i.e., <10 μs).[21] The concurrent spectral evolution provides

insight into reaction pathways in and directly following the laser-induced plasma that may be influencing this energy release.

Aluminum (Al) is a common additive of interest in energetic applications due to its high gravimetric and volumetric energy content.[22] Numerous experimental and computational studies have examined Al combustion[23–30] or detonation in anaerobic conditions (e.g., carbon dioxide [CO_2], nitrogen [N_2], water [H_2O], and other mixtures). Previous work from this laboratory provided initial insights into the effect of ambient gas for Al in laser-induced plasma conditions, but with more crude environmental control.[12,31] Others have studied laser-induced plasmas of Al in inert gases, air, gas mixtures, and vacuum.[32–35] Kwapis et al.[36] recently treated an Al laser-induced plasma as a reactive fireball that can be modeled by HyBurn (a code validated for detonation/blasts), which is a significant step in understanding how laser-induced plasmas relate to energetic phenomena. Kautz et al.[37] recently studied Al nanoparticle formation in the presence of O_2 and N_2 within a laser-induced plasma, a close analogy to this work.

This study seeks to explore the novel gas mixing capabilities to understand how reactions of a common explosive additive, Al, behave under extreme heating rates in various environments. In this study, we characterize laser-induced plasma chemistry generated from an ablated bulk Al plate within gaseous mixtures of CO_2, N_2, and argon (Ar), including spectral and laser-induced shock properties. We fix the molar concentration of CO_2 and N_2 (which are the two primarily equilibrium products from detonation on a molar basis) to the gas composition predicted by thermochemical codes for detonation of four high explosives (HEs) and fill the remainder of the mixture with Ar. We use gated ultraviolet and visible (UV/vis) emission spectroscopy to track species evolution from 100 ns to 70 µs and Z-type schlieren imaging to visualize the shock propagation. We then repeated these experiments for µm-Al powder in the four mixtures of surrogate post-detonation representation environments and air. We note that Ar tends to enhance plasma emission and temperature due to confinement, mixing, and thermal conductivity effects.[38,39] This work is a step toward understanding the effect of gas composition with and without the presence of Ar on the reactions and species evolution in and directly following Al-based plasmas.

2. Experimental Approach

A high-energy laser pulse (1064 nm, 6-ns pulse width, 900 mJ max; Quantel Brilliant B) was used to generate the laser-induced plasma. The laser was focused with a 300-mm biconvex lens through a laser window into a custom environmental chamber (Ideal Vacuum Products). This relatively long focal length can cause gas

breakdown above the focal point, and therefore the laser energy was lowered to approximately 660 mJ (~42 J/cm^2 fluence) to reduce this effect. The laser was focused just below the sample plane such that the plasma breakdown was in the powder and not the air above the sample. The focal plane was fixed for these experiments because it affects the plasma and shock properties (as shown in previous studies[40]). The laser energy/fluence was many orders of magnitude above the breakdown threshold of the material, which put our experiment in a regime of laser-material interactions in which the effects of laser absorbance by the material were mitigated because the plasma shielding dominates.[41]

The environmental chamber consisted of two quartz-side viewing windows through which the laser-induced shock wave could be imaged using schlieren imaging.[42] The chamber had flanged fiber optic feedthroughs, gas in, vacuum out, vent, and vacuum check valves. The latter was used as a pressure relief valve as a safety precaution to prevent over-pressurization (0.3-psi blowoff threshold above room pressure). For experiments that used the powder samples, a small battery-powered HEPA filter was placed inside the chamber to filter the environment from dispersed/floating particles between laser shots. The gas environment was controlled using three mass flow controllers with an automated mixing module (Alicat Scientific). For each gas combination, the chamber was purged (~0.1 Torr) and backfilled to 1 atm with the desired gas three times to reduce gas impurities. Figure 1 shows the experimental apparatus. Table 1 lists the gas combinations used and the HEs they represent. The molar fraction of CO_2 and N_2 from each HE post-detonation condition was calculated using the CHEETAH 10.1 thermochemical code while the remaining molar fraction was set to Ar, when present. Ultra-high-purity (UHP) Ar (UHP, 99.999% pure) gas, food-grade CO_2 (99.9% pure), and UHP-grade N_2 were used as the input gases.

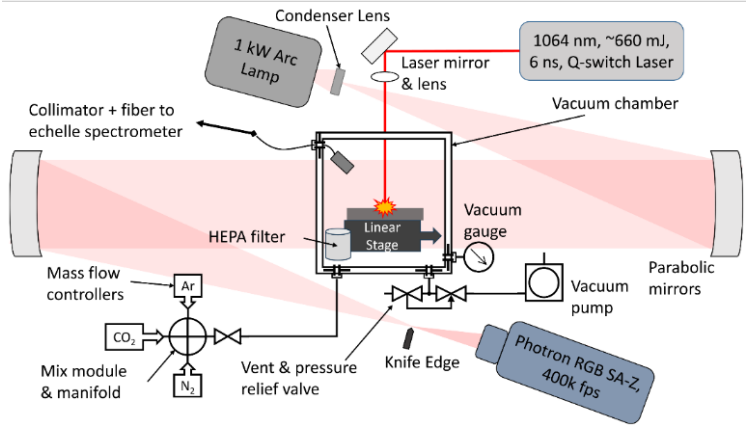

Fig. 1 Schematic of the experimental apparatus including schlieren imaging, vacuum/gas mixing system, and other diagnostics

Table 1 Gas molar compositions for each of the environments and the corresponding HE labelling scheme (no HE used in this study). When Ar is removed from the system, the CO_2/N_2 ratio is maintained. Speed of sound (v_s) for each gas combination was calculated via the simple rule of mixtures.

Environmental label	CO_2 (mol%)	N_2 (mol%)	Ar (mol%)	CO_2/N_2	v_s w/ Ar (m/s)	v_s w/o Ar (m/s)
Air	~0.04	~78.1	~0.9	<<1	343	343
CO_2	100	0	0	N/A	N/A	280
N_2	0	100	0	N/A	N/A	354.4
Ar	0	0	100	N/A	323	N/A
TNT	15.2	12.7	72.1	1.195	320.5	313.9
RDX	15.1	28.8	56.1	0.524	325.6	328.8
HMX	14.8	28.3	56.9	0.523	325.5	328.9
CL-20	25.7	34.6	39.7	0.743	322.8	322.7

For the μm-Al samples, the powder (<5 μm-Al, 99.5% pure; Sigma-Aldrich) was affixed to double-sided tape, which was attached to a glass slide set 1–2 mm above the laser focus. One advantage of this preparation method is that only milligram quantities of materials are required—we have not observed a significant difference in air shock velocity as a function of the quantity of material on the slide (since excess material is ejected away from the initial microsecond-timescale interaction region).[43] The sample position was moved between each shot to fresh material using a motorized linear stage. The plate Al sample was 99.999% pure Al (McMaster Carr) and was not moved between shots (after an initial surface cleaning shot). Both sample types were stored in a dry desiccator box before transferring into the environmental chamber.

A Z-type schlieren imaging setup (Photron SA-Z, 400,000 fps, monochromatic, 160-ns exposure time) with a broadband arc lamp (Hg-Xe, 1 kW; Newport Model #66923) was used to measure the laser-induced shock position and velocity. To generate a statistical dataset of shock velocity measurements, approximately 20 shots were collected per sample. Each image was analyzed with a custom, automated MATLAB code wherein the shock position and velocity were defined by a maxima in the schlieren intensity gradient as a function of time in the direction of propagation of the shock wave (for more details, see Gottfried and Wainwright[21]). Laser-induced shock velocity measurements were pulled from the 1-D sum of the center approximately 24 pixels from these frames to reduce the effect of shock-wave curvature on the measurement. Although there are many methods to define the characteristic air shock velocity for a given energetic sample,[21] here we define it at a fixed time step of 13 μs following the laser pulse using a TNT blast model fit to the expansion of these laser-induced plasma shock waves.[44] We found that defining the characteristic shock velocity at 13 μs reduces the shot-to-shot error in the shock-wave measurement but decreases the absolute value difference between samples compared to other fitting methods.

The spectral data were collected from two instruments with varying sensitivities over the spectral range from 200 to 1,000 nm. In the first case, a UV/vis echelle spectrometer (OWL-325/65, average $\lambda/\Delta\lambda = 3955$ across the spectral range of 250–760 nm; Catalina Scientific) coupled to a gated intensified charge-coupled device (ICCD) (Condor ICCD, 14-bit, 100 ns minimum gate width; Raptor Photonics) was used as a UV-sensitive detector with fast gating capabilities. Spectra were stepped through time by adjusting the trigger delay time through a digital delay generator (Stanford Research DG535) synced with the Q-switch output of the laser. The following timesteps and gate widths were used: 100-, 400-, and 700-ns delays with a gate width of 100 ns; 1-, 4-, and 7-µs delays with a gate width of 200 ns; 10-, 40-, and 70-µs delays with a gate width of 500 ns. These are significantly shorter gate widths than previously published by this group due to the high sensitivity of this ICCD. In follow-up experiments, Ar was removed from the gas mixtures and a separate spectrometer was used with greater near-IR sensitivity. This second spectrometer is an echelle (EMU-120/65, average $\lambda/\Delta\lambda = 6936$ across the spectral range of 253–912 nm; Catalina Scientific) coupled to a slower electron-multiplying charge-coupled device (Andor iXon +885) with a minimum gate width of 10 µs. Data from this second spectrometer was collected from the 1- to 10-µs time window without stepping through time and is considerably more sensitive in the >600-nm region that contains N I and O I lines of interest. Ten laser shots were collected at each timestep/gas combination for both spectrometers. All error bars displayed on figures throughout this work represent 95% confidence intervals (CIs) among the multiple shots collected for each diagnostic.

3. Results

3.1 Plasma Spectroscopy with Ar

Figure 2 compares the temporal evolution of the intensity-corrected emission spectra for plate Al in several environments, with several species of note observed including Al I, A1 II, and H. C I, C II, and N II are present in the relevant environments containing these elements to approximately 400 ns; N II and C II have not been observed previously under these experimental conditions conducted primarily in air due to relatively long gate delay times. Future work is required to determine whether the presence of N II is due to vacuum UV photo-ionization/radiation or prompt electron excitation.[45,46] In systems containing Ar, there is a high density of Ar I and Ar II peaks, which are present between approximately 350 and 550 nm, which have not been individually identified for this study. These Ar peaks dissipate by approximately 1 µs and are not strongly present in each environmental case and therefore were not used for plasma temperature

(Boltzmann and Saha-Boltzmann) calculations (see Discussion section). The spectral evolution of the plate Al in HMX and RDX, and μm-Al in its environments, looks qualitatively similar. When oxygen is present, aluminum oxide (AlO) can be weakly observed at times >40 μs; the magnitude of AlO intensity for μm-Al powders is larger than for the plate Al, consistent with our previous work.[16] AlO will theoretically not spontaneously form within the plasma until it cools (kinetically) to approximately 5000 K.[47]

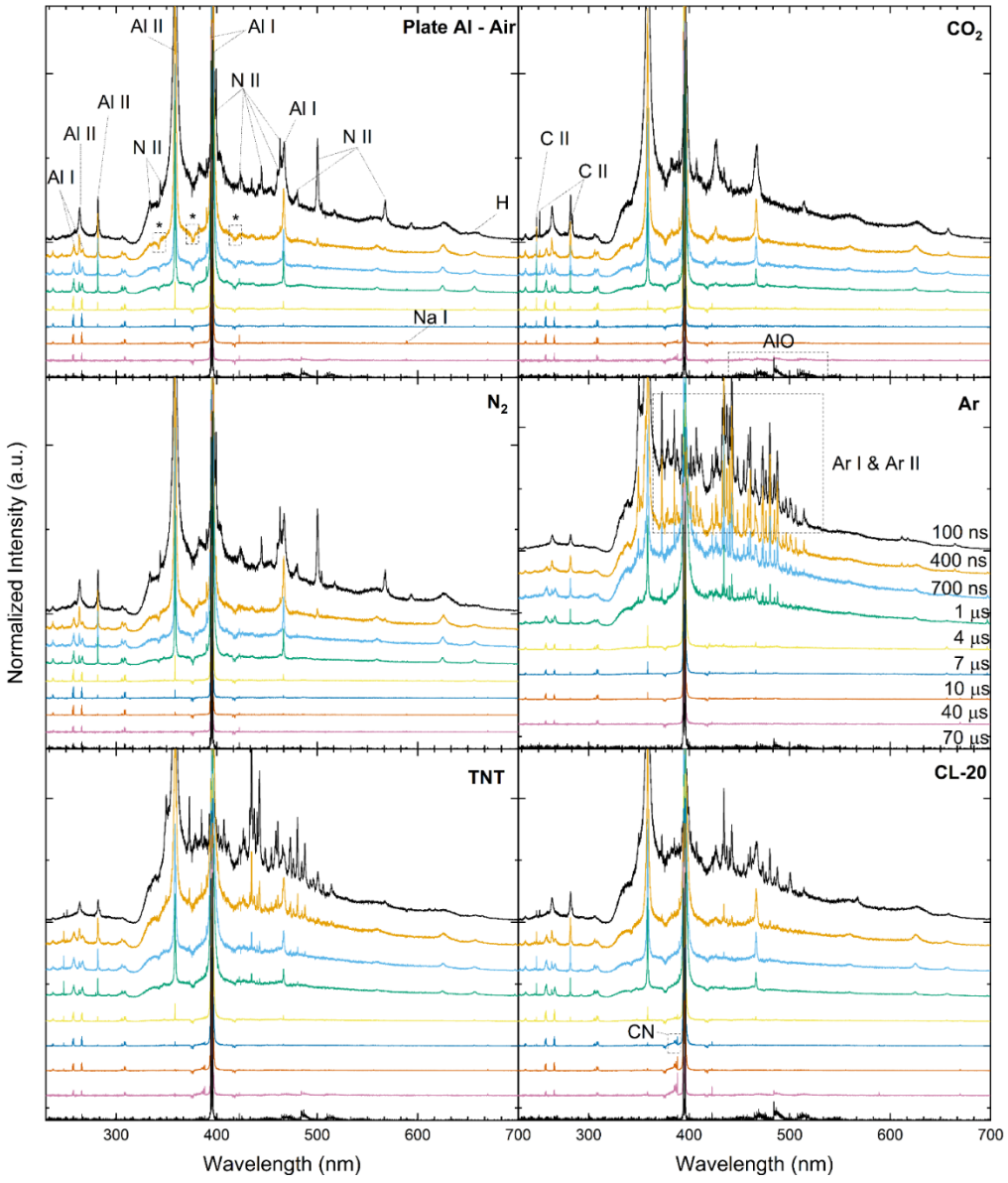

Fig. 2 Normalized intensity-corrected spectra with vertical offset representing the various timesteps for plate Al in several environments. Species are denoted on the figure. Several artifacts from the spectrometer grating/blaze correction are denoted in (*).

Figure 3 shows a magnified view of the temporal evolution of primary Al I and Al II peaks of interest. Self-reversal[48] is observed for the 396-nm Al I ground-state transition peak at times 4 µs, which implies an optically thick plasma over the timescales observed. Self-reversal is also observed for the 308-nm (ground state transition) Al I peak out to times of approximately 1 µs. There appears to be a slight Stark shift of the peak position at times <4 µs for these and other peaks. Significant Stark broadening, along with poorer signal-to-noise ratio (SNR) due to reverse-bremsstrahlung continuum emission, is present for these peaks. The SNR improves over time. A strong Ca II peak (393.3 nm) emerges from the continuum emission at approximately 1 µs and then persists through the plasma lifetime. Ca II at 396.8 nm is not observed at similar timescales but is likely within the noise and convoluting with the Al I peak at 396.2 nm at times <4 µs.

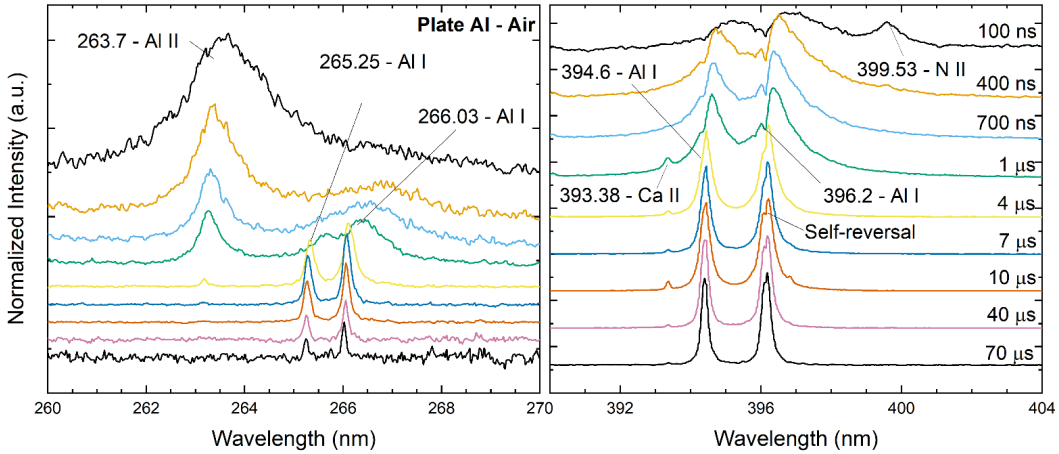

Fig. 3 Al I and Al II peak tracking for plate Al in air

We tracked the intensity of several peaks of interest as a function of time, including C I (248 nm), carbon nitride (CN) (integrated intensity from 384 to 388 nm), and AlO (integrated intensity from 484 to 500 nm) (Figs. 4 and 5). We did not observe the potentially convoluting H_β line at 486 nm. There are no visible peaks for these species in the N_2 and air cases in the intensity-corrected spectra; thus, the responses in those two environments represent the lower detection limits (e.g., background intensity at that wavelength). This background intensity is higher for the pure Ar environment, which is a result of signal intensity enhancement for pure Ar over the other gases, as observed elsewhere (e.g., Kuzuya et al.[49]). Unsurprisingly, the CO_2 environment has the highest C I intensity across all times and samples. Note that the µm-Al samples appear to have a higher C I intensity in the detonation gas mixtures than the plate samples until approximately 40 µs as well. The intensity appears to be roughly constant for the post-detonation gases (and CO_2) until approximately 1 µs when it begins to exponentially decay (approximately linear on these log-log axes). The signal is essentially lost by approximately 40 µs. CN

formed through recombination reactions was commonly observed in the explosive gas mixtures at times >7 µs. The intensity of the band generally trends with CO_2 content in the gas mixture and appears stronger for the µm-Al sample than the Al plate at 10 µs. This trend is similar for the CN with the µm-Al sample as a function of CO_2 content, except that the CN is growing in intensity through the same timesteps versus decreasing in time for the Al plate. Interestingly, the CN for the TNT µm-Al sample appears to be decreasing rather than increasing across these timesteps.

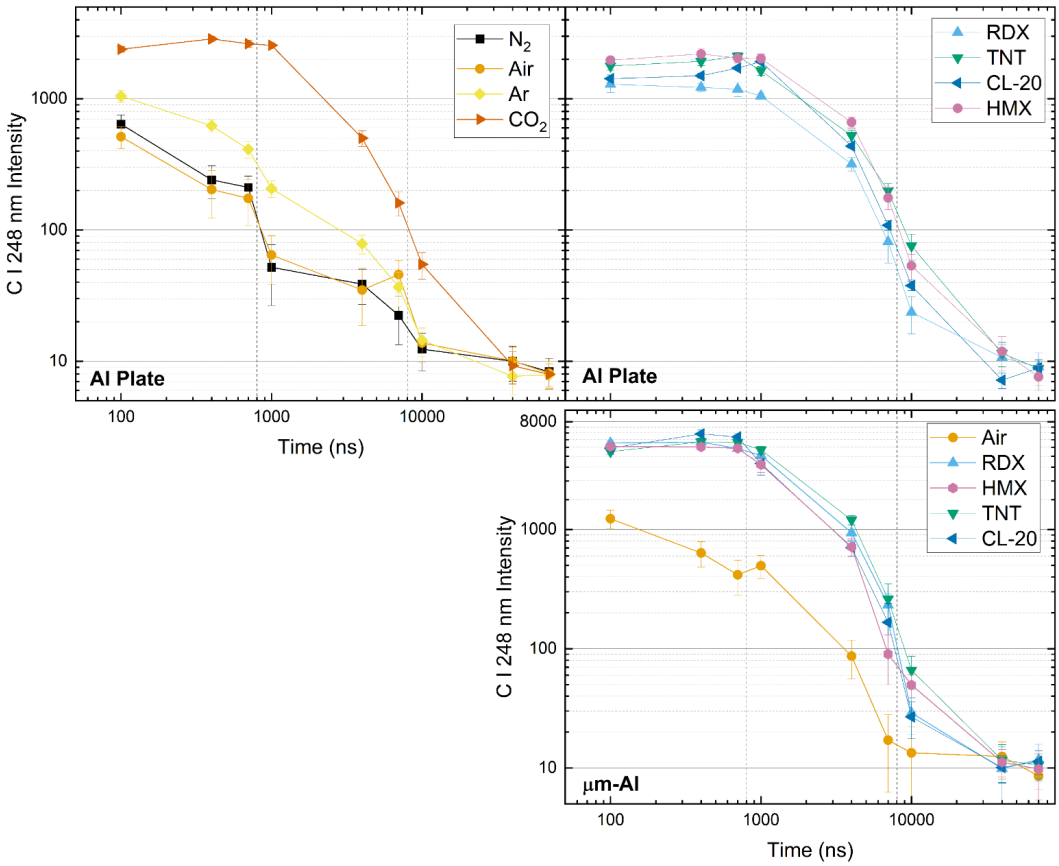

Fig. 4 Temporal evolution of C I for plate Al and µm-Al. N_2, air, and Ar traces represent the background intensity at this wavelength.

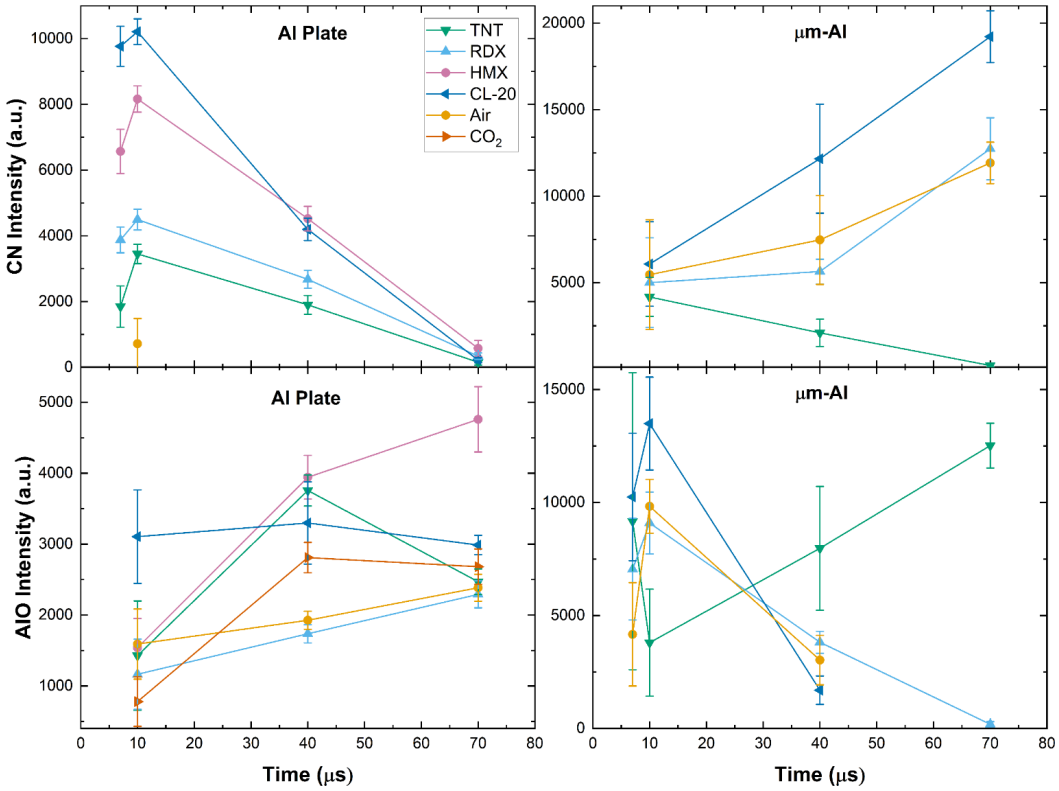

Fig. 5 CN and AlO intensity for plate Al and μm-Al for the four post-detonation gas environments. Data shown for available timesteps when SNR was acceptable.

The AlO intensity, like CN, is significantly stronger for μm-Al than Al plate. For the plate samples, it appears that the CL-20 environment has the strongest AlO signal at early times, which persists throughout 70 μs. The remaining Al plate samples appear to be growing in intensity throughout the tens of microsecond timeframe, which is consistent with previous results.[16] Interestingly, the HMX post-detonation gas produces stronger AlO emission at later times for the Al plate than the other ambient environments, despite having less available oxygen for reaction than other samples such as CO_2 or CL-20. For the μm-Al sample, the AlO signal appears to peak at approximately 10 μs and steadily decreases from there. Similar to the CN case, the TNT μm-Al sample displays the opposite trend of the other samples in that it appears to continue to increase by 70 μs (while producing significantly less AlO emission at earlier times). TNT is the most oxygen-deficient explosive (i.e., fuel-rich) of the four, whereas CL-20 has the highest oxygen balance (and highest peak AlO at approximately 10 μs).

Electron densities can be calculated via Stark broadening of peaks given that the proper broadening parameters are known. The approach has been described previously[16] and uses the available broadening (Stark) parameters from Konjević and Wiese[50] and Griem[51]. We calculate the electron density using three separate

lines (H at 656 nm, Al II at 281 nm, and Al II at 358 nm) to 4 μs, whereafter the SNR for these species drops considerably. The electron densities are shown in Fig. 6 for Al plate and Fig. 7 for μm-Al. Al particles have Al_2O_3 shells that are 3 to 6 nm thick, for example.[52] For the μm-Al particles, some C and H may be from functionalized or hydrated species on this Al_2O_3 surface, which have been observed for commercially available Al particles.[53] Another contributor to H peaks may be due to the small impurity fraction of H or H_2O within the CO_2 tank (0.1%) and residual air not removed during the cyclic purge-fill cycles, although some work suggests that humidity levels must be significantly elevated to observe H from H_2O as the source.[54] H peaks were not observed in the Ar case, which broadly suggests that the H is from environmental effects. It appears that the electron density measurements derived from 358-nm Al II and H broadening corroborate each other, with the measurement made from 281-nm Al II resulting in nearly an order lower value at similar timesteps. This difference could be due to an error in the Stark impact broadening parameter for this line. The electron density in the Ar environments (as measured from the Al II peaks) is higher across almost all timesteps than in the other environments. Using the 358-nm Al II measurements (given their consistency with H and small shot-to-shot variation), we estimate the electron density for plate Al to decrease from approximately 6×10^{18} cm^{-3} at 100 ns to approximately 3×10^{17} cm^{-3} at 4 μs with only minor differences as a function of gas composition. For μm-Al, we estimate the electron density ranges from approximately 5×10^{18} cm^{-3} at 100 ns to widely varying values at 4 μs, an interesting deviation from the plate Al. The electron density among the μm-Al samples at 4 μs appears to trend roughly as a function of Ar content within the gas mixture, with lower Ar content having higher electron densities. This is the opposite trend observed for the Al plate in which the pure Ar gas had the highest values among all samples. Given that "inert" samples in previous work (e.g., Al_2O_3 powder from Wainwright et al.[16]) had higher electron density than Al powder, this work suggests a major effect of Ar on the electron density and perhaps material reactivity.

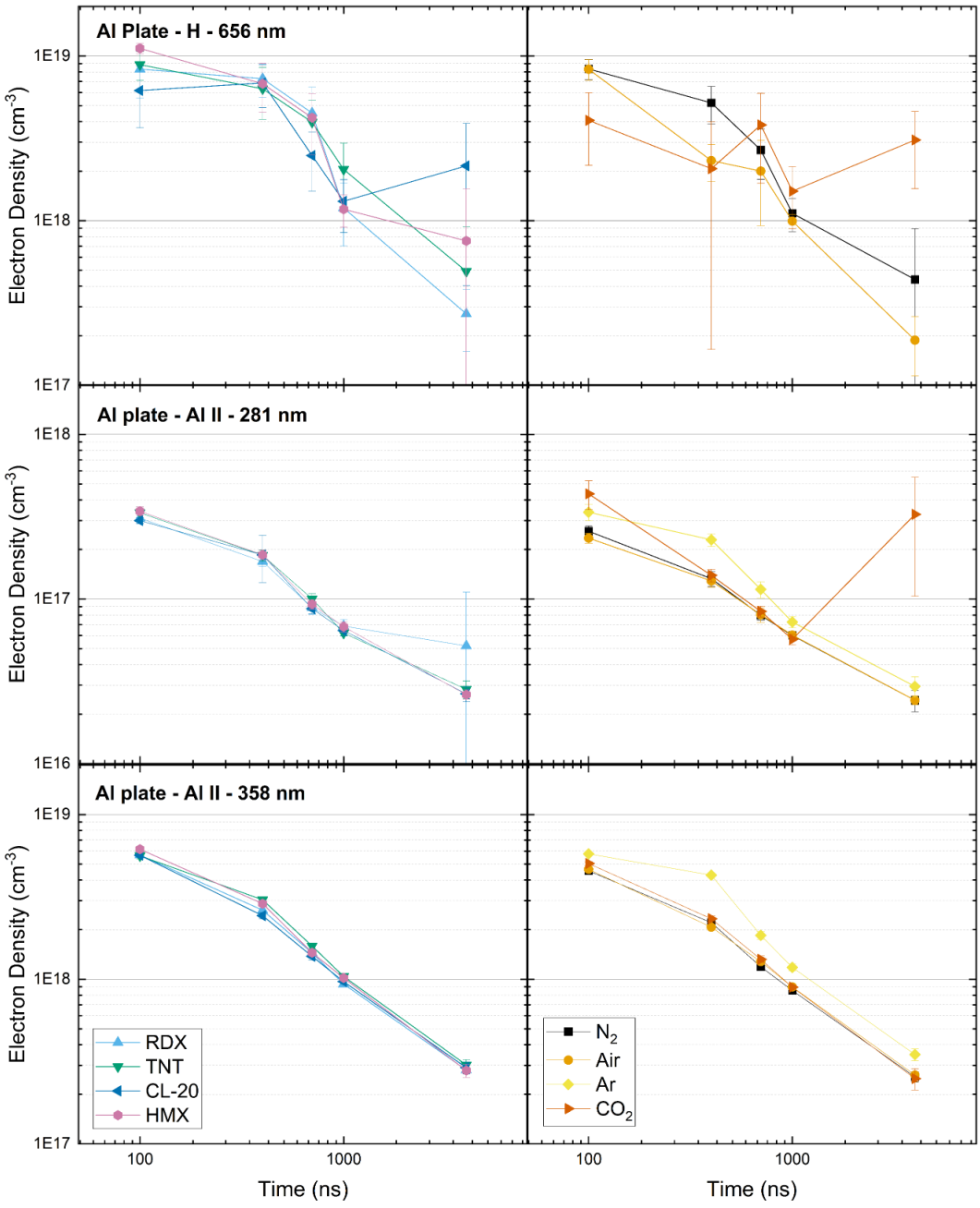

Fig. 6 Electron density as a function of time for plate Al, as derived from H_α, Al II (281 nm), and Al II (358 nm) peak (Stark) broadening

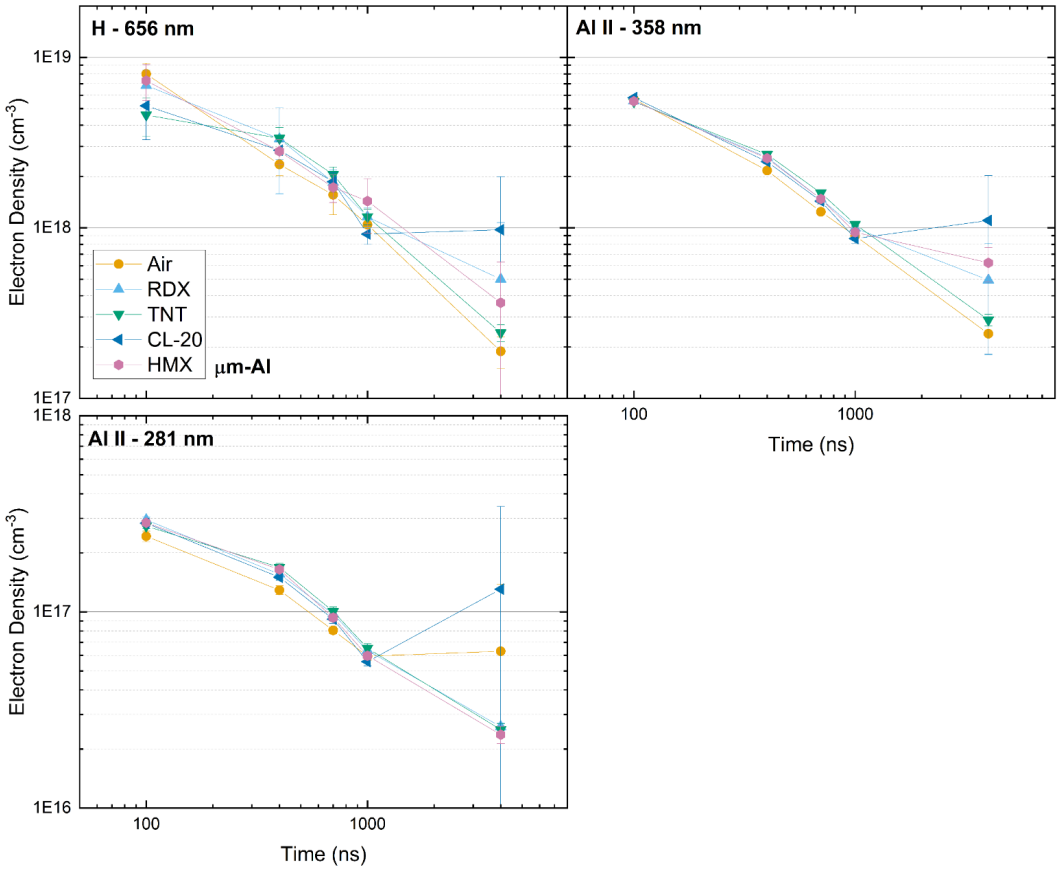

Fig. 7 Electron density as a function of time for µm-Al, as derived from H_α, Al II (281 nm), and Al II (358 nm) peak (Stark) broadening

To further investigate the effect of Ar on the electron densities, we have selected two timesteps for plate Al and displayed them as a function of Ar content (Fig. 8). We observe monotonically increasing electron density as a function of Ar content at 700 ns, with some variability of the same trend at the earlier timestep of 100 ns. The measurements derived from the Al II 281- and 358-nm peaks generally fall within the 95% CI of the other measurements. The HMX and RDX gas compositions are very similar, which is reflected in the similarity in their electron density measurements at both timesteps. The Al II/Al I peak intensity ratio at two timesteps is also displayed as a function of Ar% (Fig. 9). At the early time of 100 ns, the trend is nearly exponential as Ar% increases, but then the correlation between this value breaks down at 700 ns as the intensity of Al I overtakes Al II.

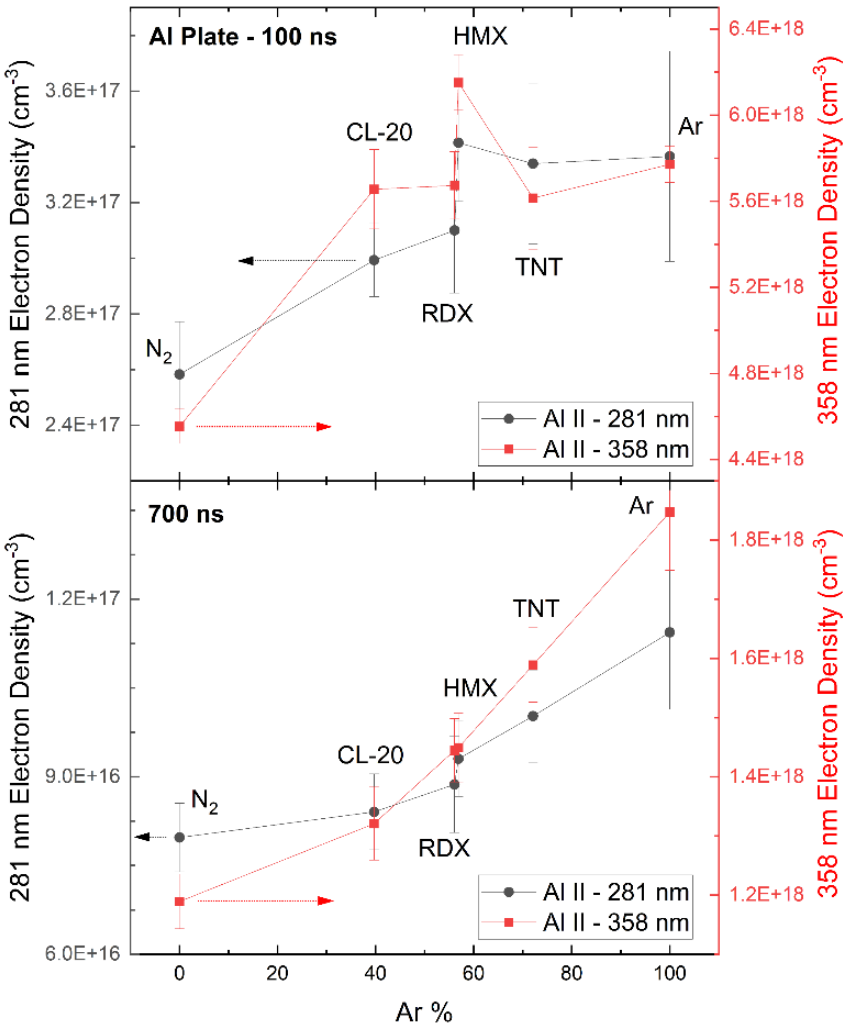

Fig. 8 Electron density as a function of Ar% derived from II peaks (281 and 358 nm) in the various gas mixtures for plate at two timesteps

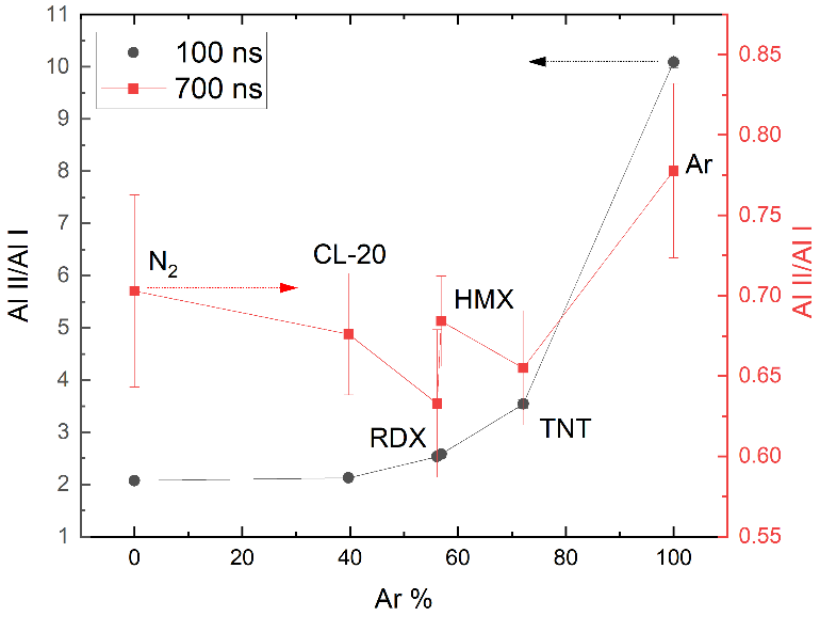

Fig. 9 Al II/Al I peak intensity ratio as a function of Ar% at two timesteps for plate Al

Using the Boltzmann and Saha-Boltzmann plot method,[55,56] we are able to estimate the excitation and electron temperature within the plasma and known spectroscopic constants available at Kramida et al.[57] Lines used for this calculation are shown in Table 2. A thorough, recent discussion of this method is found in Bousquet et al.[58] For these calculations, a self-absorption correction was performed for the 396.15-nm Al I line, following the methodology laid out in the Supplementary Materials section of Wainwright et al.[16] These Boltzmann fitting methods generally have large errors (on the order of 10%–30%, a full discussion of sources are in El Sherbini et al.[59]) that have been omitted from the plot for clarity. Difficulty discriminating between samples could be due to the reduced sensitivity of the Boltzmann method as excitation temperature increases.[58] Thus, differentiating the plasma temperature between the samples becomes difficult after approximately 1 µs using this experimental configuration, and all measured temperatures should be taken as relative rather than absolute. These plasma excitation temperature measurements are shown in Fig. 10. Using the Boltzmann method, we generally find excitation temperatures from 50,000 to 5,000 K, with CO_2 and N_2 having the highest temperatures and air and TNT having the lowest. Electron temperatures measured via the Saha–Boltzmann method are significantly higher, ranging from 130,000 to 40,000 K over the same time window. The mismatch in these measurements has been observed in previous work and implies a plasma that is not in LTE. The discontinuity in both temperature traces is likely a result of the change in gate width between the 700- and 1,000-ns time steps.

Table 2 **Selected Al I and Al II lines and their spectroscopic parameters used for the Boltzmann method temperature measurements. Al II species were used in Saha-Boltzmann measurements of the same spectra.**

Species	Line (nm)	$E_{j,\,upper}$ (cm^{-1})	Transition probability A (s^{-1})	g_{upper}
Al I	237.21	42237.783	5.76E+06	2
Al I	257.51	38929.413	5.99E+06	4
Al I[a]	265.25	37689.407	1.42E+07	2
Al I[a]	266.04	37689.407	2.84E+07	2
Al I	394.40	25347.756	9.85E+07	2
Al I	396.15	25347.756	4.99E+07	2
Al II	263.76	133450.07	2.85E+07	9
Al II	281.61	95350.6	3.57E+08	1
Al II	358.65	123423.36	2.35E+08	9

[a] Species are used from 1 μs and beyond where SNR was improved.

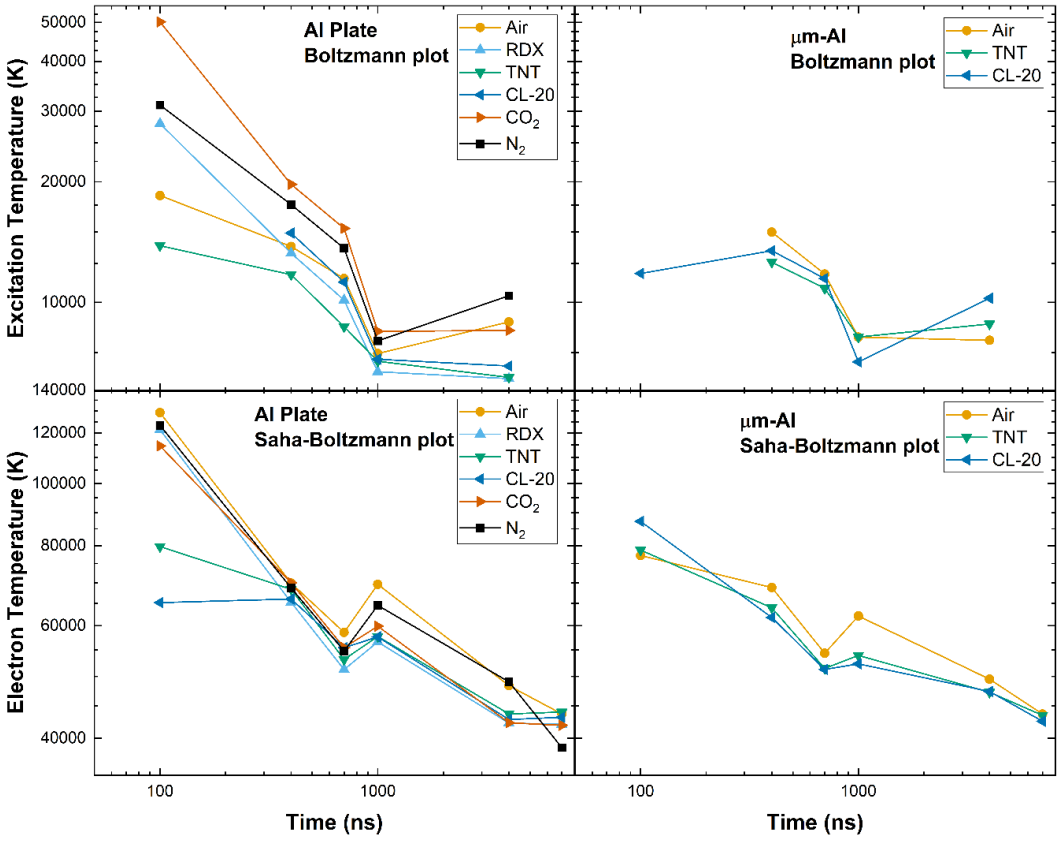

Fig. 10 **Plasma excitation temperature as derived from the Boltzmann and Saha-Boltzmann plot methods from selected Al I and Al II peaks for plate and μm-Al, where possible. Some timesteps are omitted due to convolution of lines, poor SNR, etc.**

3.2 Plasma Spectroscopy without Ar

In the second series of experiments, Ar was removed from the system and the spectrometer was swapped to a visible/near-IR sensitive unit with a minimum 10-µs time window. Average intensity-corrected emission peaks for several species of interest at >650 nm are shown in Fig. 11, where N I, O I, and C I peaks, which were not observable previously, are revealed. We observe stronger relative H peaks for each µm-Al sample compared to the plate Al, suggesting the material itself is the likely source of H with smaller effects from environmental impurities. We can track the intensity of the strongest N I line (868.1 nm) and O I (777 nm) as a function of input N and O input molar fraction for both samples (Fig. 12). The N I peak intensity generally trends with input composition, implying there is little in terms of gas-phase reactions gettering or consuming N within the 1- to 10-µs time window. However, the O I peak intensity does not appear to directly trend with the effective molar O input concentration for either sample, providing secondary evidence of reactions occurring and affecting the O I intensity. The data point for the CO_2 composition represents background intensity because, as expected, this N I peak is not observed. There is no significant statistical difference between the RDX and HMX intensity for both samples, and the powder appears to exceed the plate Al in intensity in all cases. Interestingly, the intensity for the pure N_2 case drops relative to air for the plate Al; this process is similar for the µm-Al.

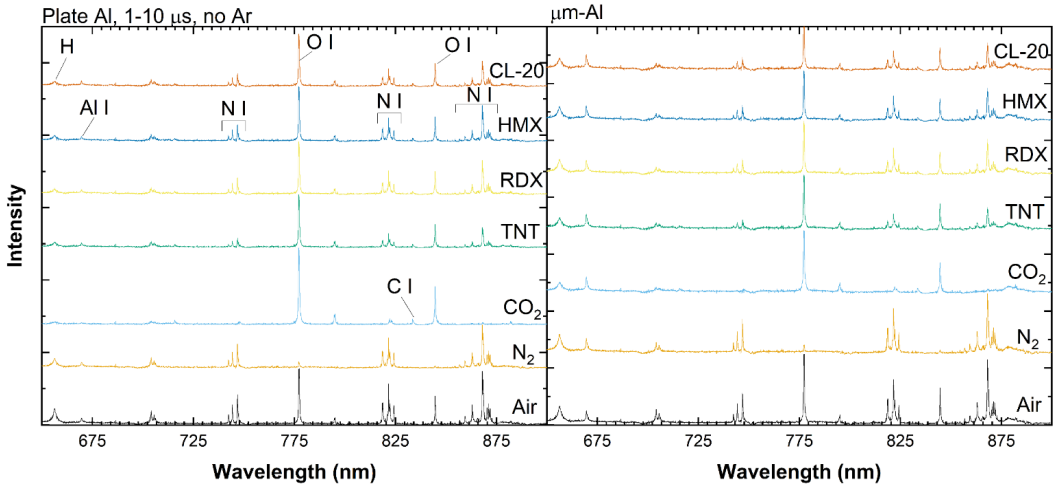

Fig. 11 Averaged intensity-corrected spectral emission peaks at >650 nm gated from 1 to 11 µs for both Al samples

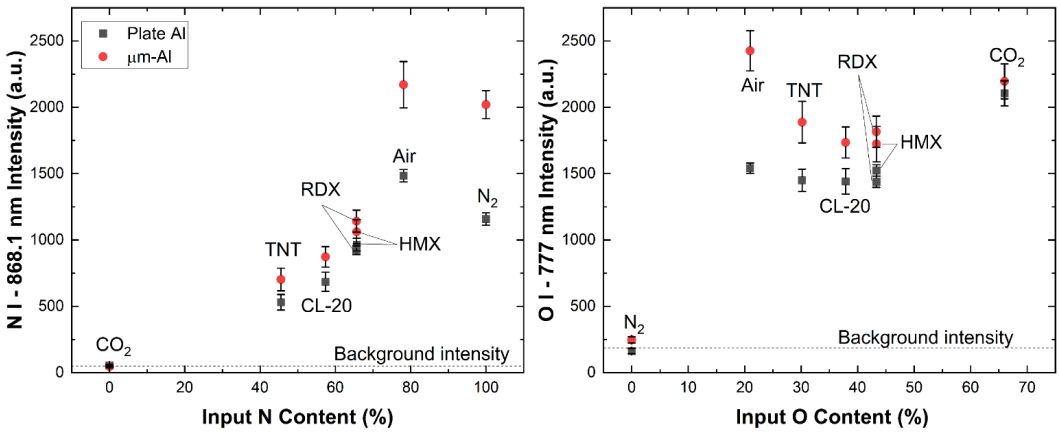

Fig. 12 Corrected intensity of N I (868.1 nm) and O I (777 nm) peaks as a function of N_2 content (e.g., direct gas mixture composition) and O (e.g., effective molar% from CO_2) in the ambient gas for both plate Al and µm-Al from 1 to 11 µs

The ratio of peak intensities over a fixed time window of 10 µs may provide some insight into the reactions of various species within the laser-induced plasma. Four examples of intensity ratios, including Al/N, Al/O, O/N, and Al II/Al I (ionization ratio), are shown (Fig. 13), with the specific emission lines denoted. Several interesting observations can be made from these simple comparisons.

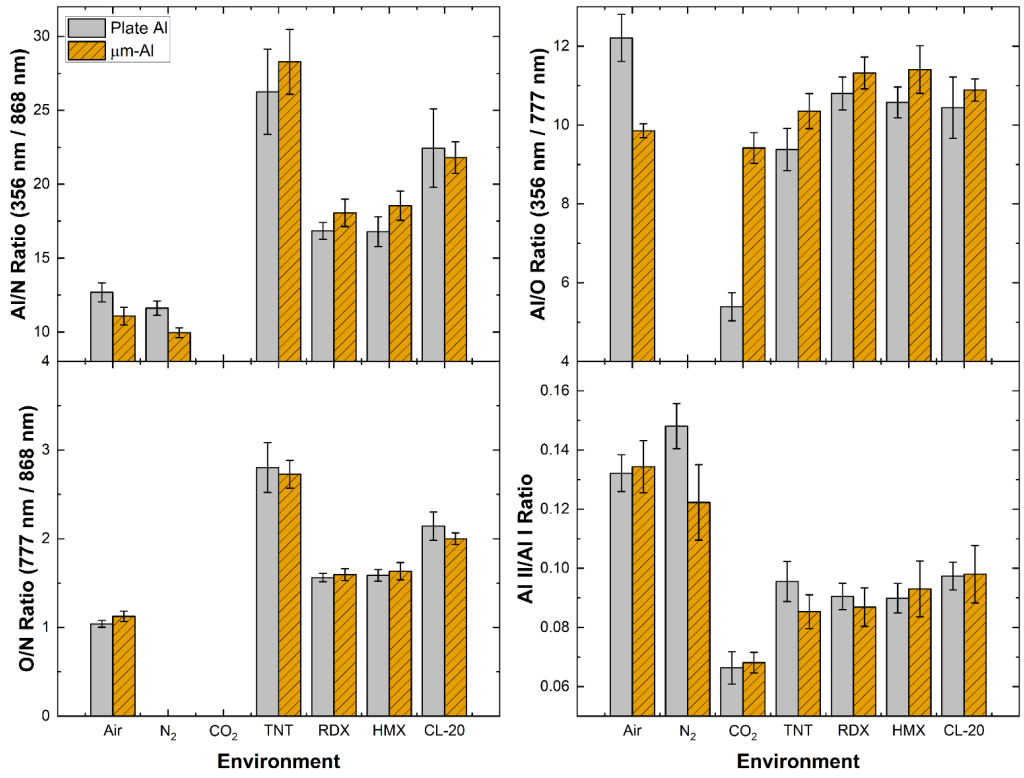

Fig. 13 Ratio of averaged intensity-corrected emission peaks over the 1- to 10-µs time window without Ar. Data that is missing is because the sample gas combination does not contain a ratio species.

First, for the Al/N ratio, there is a reversal from the air and N_2 cases to the explosive cases from the plate to the μm-Al in the larger-intensity ratio, where, for the latter two cases, the ratio is smaller for the powders and larger for the plate (reversed for the HE gas combinations). This implies that either the Al peak is stronger or the N I peak is weaker for the μm-Al. We note that thermodynamically AlN (g), a potential getter for gas phase N, is not energetically favorable to form at temperatures below 6,000 K, but that the condensed phase AlN (s) can form below 2,800 K.[47] However, recent work has directly observed the formation of AlN in and post-mortem from Al plasmas in N_2,[37] suggesting similar AlN (g) → AlN (s) pathways could be also occurring here. Similar AlN bands were not observed here, but this may be due to low SNR for this species. No attempts were made to recover and characterize residue or products from the plasma.

Second, for the Al/O ratio, we find that the powders exceed the plates for all cases except air, where either weaker Al peaks and/or stronger O peaks result in the powder having a lower ratio than the plate. The increase in O peak intensities for μm-Al from Fig. 12 implies the latter. The ionization ratio also appears similar between the two samples, which may be a result of the time-averaged measurement; only the N_2 shows a difference between the plate and μm-Al, with the latter having a lower ratio than the former.

4. Laser-Induced Shock Velocity Measurements

The laser-induced plasma and resulting shock wave for several representative gases of interest are shown in Fig. 14. For the first several microseconds, the plasma saturates the camera, then evolves into emissive species, particularly at times >10 μs, where species emitting in the blue (assumed to be AlO at 486 nm) become apparent and are visible in that channel of the color camera. Continued evolution of the gaseous plume is visible out to hundreds of microseconds. Environments with reduced oxygen (e.g., N_2) display reduced AlO emission at tens of microsecond timescales, but continued atomic Al emission (~400 nm/violet light) is observed. The images for the RDX and HMX gas mixture samples look qualitatively similar to those for CL-20 and TNT (Fig. 2).

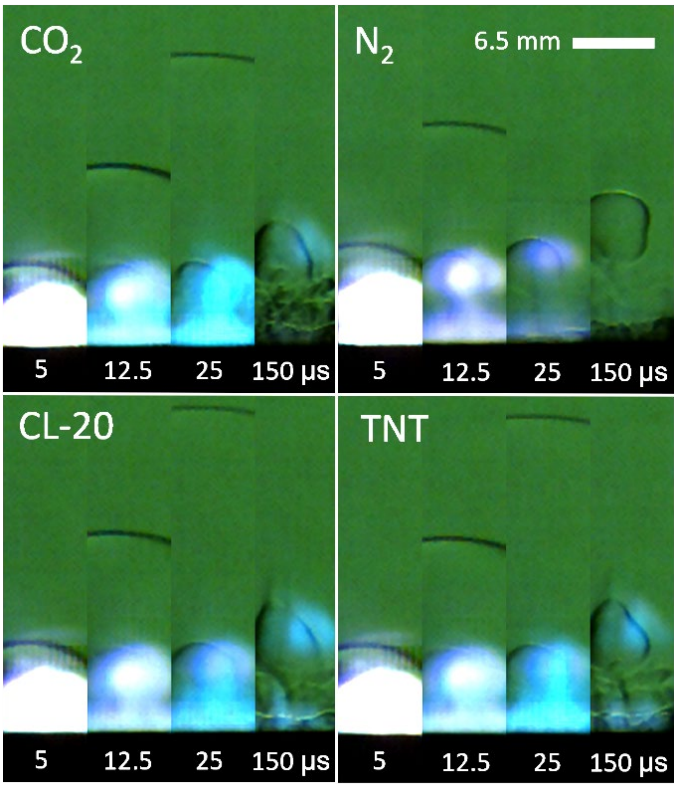

Fig. 14 Stills from representative schlieren videos demonstrating shock-wave propagation and plasma emission for several gases with the µm-Al sample. Scale bar applies to all images.

The laser-induced shock velocities for these two samples in the mixed environments (including Ar) are presented in Fig. 15 as both a sample-to-sample bar comparison and as normalized to the speed of sound of the gas mixture (v_s) plotted as a function of Ar% within said mixture. Among the plate Al samples, we find that the 100% Ar case has the highest shock velocity, despite having the second slowest v_s and no oxidants or nitrogen to provide the plasma for reaction, which may be due to enhancement in the plasma properties such as higher ionization and higher electron densities outcompeting the lack of chemical reactants. In general, Ar appears to introduce significant variation in the relative shock velocities, an unexpected result that will be discussed later. Moving from pure N_2 to CO_2, we see a dramatic increase in the v_s-normalized shock velocities despite the CO_2 having the slowest v_s. Among the post-detonation gas mixtures with Ar, after normalizing for v_s, there is little correlation among the samples with either Ar, CO_2, or N_2 content, as evidenced by the stark difference measured between the RDX and HMX samples, despite their similarity in environments. We find that in all cases, the µm-Al produces a faster shock velocity than the plate Al. The reversed trend of TNT and CL-20 environments with both plate and Al powder once again suggests Ar is playing a role in reactions, recombination, and the microsecond energy release.

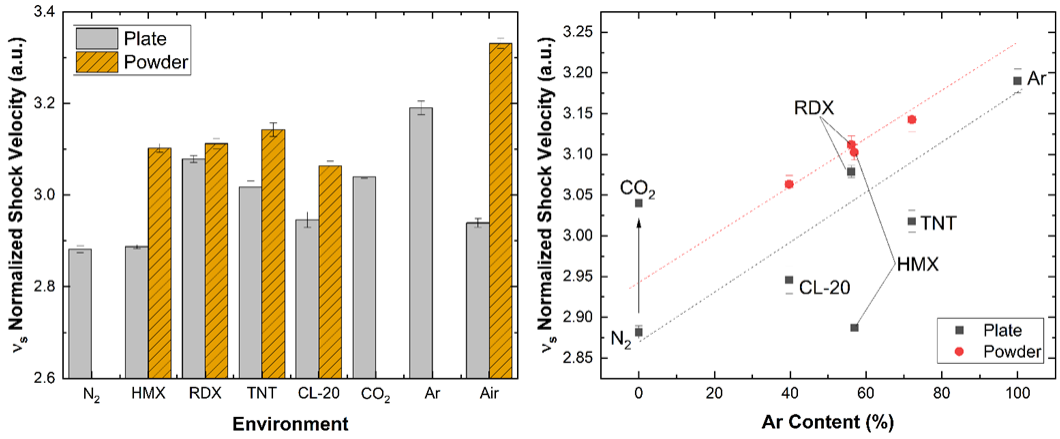

Fig. 15 Laser-induced shock velocities, normalized to the speed of sound of the given gas mixture, as a function of Al morphology (left) and Ar% within the gas mixture (right)

An example of the shock progression from the strong to weak (acoustic) shock limit is shown in Fig. 16. Here, the shock-wave Mach number evolution (using the speed of sound of each mixture) is shown for several environments with µm-Al without Ar for several samples. The Mach number is specific to the environment, as calculated from a simple rule of mixtures and listed in Table 1. Interestingly, the µm-Al in the CO_2 case begins at the fastest Mach number and then falls below air at later times, which implies a change in the shape of this curve. Furthermore, there is a bifurcation that occurs between the CL-20 and N_2 curves, where they begin at similar Mach numbers, but the N_2 result is higher by the end of the curve. The change in curvature of this decay may be due to continued energy release and deviation from the instantaneous energy/mass release assumption classically used in the Sedov–Taylor–Von Neumann analyses of shock waves from laser-induced plasmas.

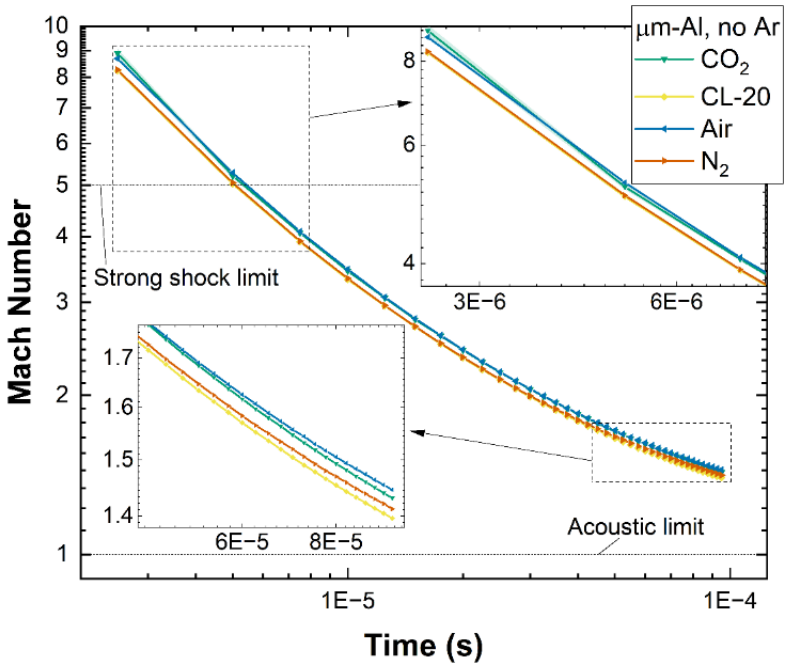

Fig. 16 Mach number evolution (using the speed of sound of each mixture) for several environments with µm-Al without Ar

Relative laser-induced shock velocity measurements for the two samples in the various environments without Ar are shown in Fig. 17, normalized to the CO_2 data point (slowest for both cases) and displayed as a function of speed of sound for each medium. The powder sample has a faster relative shock velocity for all environmental cases, similar to the Ar-containing environments. The relationship of a characteristic relative velocity for both samples with speed of sound is well represented by a quadratic curve, except for the air/µm-Al case, which has a significantly higher shock velocity than the trend.

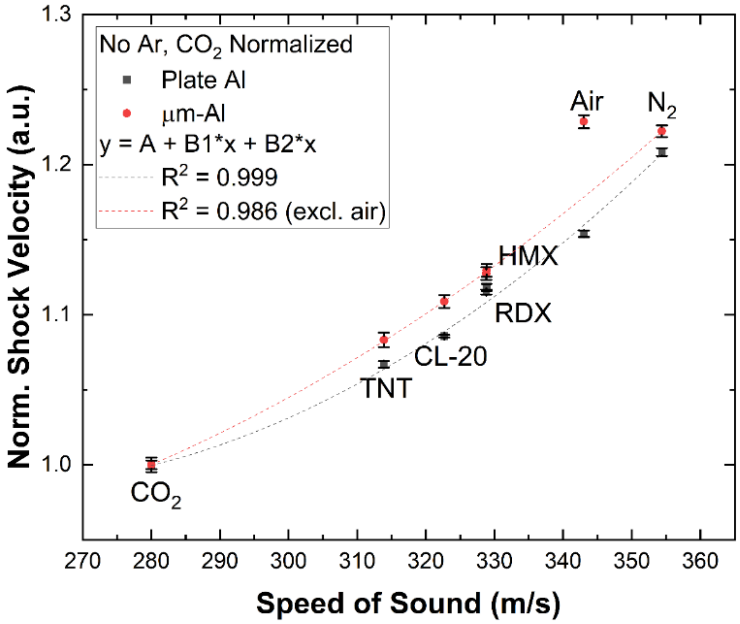

Fig. 17 Laser-induced shock velocity (result of the Dewey fitting to the experimental data at 13 µs) as a function of the native speed of sound of the gas mixture for plate and µm-Al without Ar, normalized to the CO_2 velocity (e.g., lowest for both samples). Quadratic fittings are shown as a well-fit relationship between the quantities.

Figure 18 shows a comparison across environments rather than samples. It illustrates the relative laser-induced shock velocities for the plate Al with and without Ar, where two main characteristics are noted: (1) the presence of Ar causes a stochastic variation among the samples and (2) the removal of Ar causes a general increase in the relative shock velocity across all samples. These data imply the presence or concentration of various CO_2, O_2 (air), or N_2 components (and therefore O and N concentration) has minimal effect compared to the general speed of sound of the media, at least for the Al plate. However, the speed of sound of a given environmental mixture is primarily affected by the temperature, making it difficult to deconvolute the effect of reactions (dependent on O and N concentration) that heats the environment and the native speed of the sound of the mixture based on our rule of mixtures assumption.

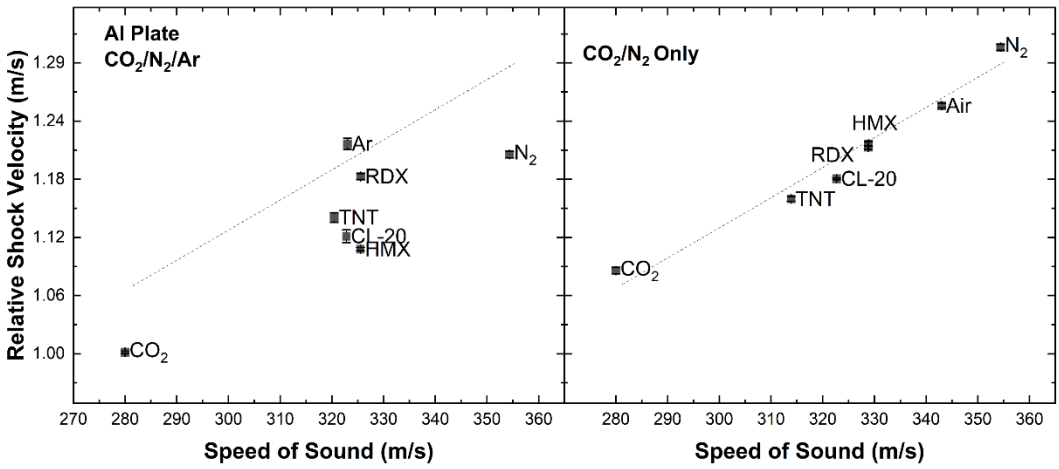

Fig. 18 Laser-induced shock velocities of Al plate, comparing compositions with similar CO_2/N_2 ratios but with and without Ar. The dotted line is a guide for the eye in both plots for ease of comparison.

5. Discussion

From the schlieren images and filtered, intensified imaging, we can observe a significant reduction in blue light that likely corresponds to AlO emission at approximately 486 nm formation at times >10 μs (e.g., the N2 environment).

Given the complexity of the dataset, the major trends with time, gas content, and sample morphology are listed in Table 3. In the presence of Ar, we find an enhancement of Al ionization ratio and electron density at times <1 μs as a function of increasing Ar content within the mixture. This trend appears to lessen moving from 100 to 700 ns, with a relative increase of the ionization ratio with time within most samples from 100 to 700 ns. Given the similarity between the electron density results from 358 (Al II line) and 656 nm (H line), and given the lack of significant H presence in several of the gas environments, we use the 358-nm measurements for comparisons between samples. In addition, there is little difference between the powder and the plate for ionization ratio. Interestingly, the plate Al in CO_2 over the same timescale has nearly an order of magnitude higher electron density, which could be a result of plasma confinement by the heavier gas.

A monatomic, quadratic relationship between speed of sound and shock velocity without Ar for plate Al implies a lesser effect of O or N concentration on early-time reactivity with Al, whereas large variations with the introduction of Ar imply early-time plasma intensity differences (e.g., density, temperature, and free electrons) that affect the shock velocity. Clearly, there is an increase in the shock velocity moving from the plate Al to μm-Al. The only evidence that this is related to available reactant species is the dramatic increase of powder in air. We speculate

that this is due to the small effect of energy loss due to ionization and bond breaking (e.g., bond disassociation free energy) that counteracts energy released from recombination—although this hypothesis needs verification via further controlled studies. For example, in an environment with equivalent moles of O but comprising O_2, CO, and CO_2, can the effect of the additional energy sink for CO_2 disassociation versus O_2 within a laser-induced plasma be established? There are also likely influences from the differing kinetic reaction rates of Al with the various gases. For example, using readily available kinetic rate constants from the National Institute of Standards and Technology (NIST) Kinetics Database[60–64] (not accounting for pressure effects), we find that Al will react more quickly with O_2 at low temperature (<1500 K) but with CO_2 above this temperature (Fig. 19). Similarly, thermodynamic driving forces for various species suggest the plasma must cool significantly for several gas phase species to form but suggest species such as AlC (g) may be preferential at higher temperatures. The same thermodynamic arguments may be limited in their utility, given that AlN (g) has been overserved from Al laser-induced plasmas[37,65,66] while also having the highest thermodynamic barriers to formation at high (e.g., plasma relevant) temperatures. Thermochemical and kinetic data for Al under relevant extreme temperatures and pressures present in this experiment is extremely sparse.

Table 3 Heuristic observations for the effect of the various environmental and sample parameters explored in this study

Property	Ar case	w/ Time	w/ Gas content	Powder vs. plate
Electron density	With Ar	~5×10^{19} cm^{-3} at 100 ns to ~2×10^{17} cm^{-3} at 7 μs as measured via 358 nm	Increasing w/Ar content. No trend w/N_2 or CO_2 content.	Plate higher as measured via 281 nm, similar as measured via 358 nm.
	Without Ar	Average ~2 to 9×10^{18} cm^{-3} from 1 to 11 μs	Similar as measured via 358 nm. No trend w/N_2 or CO_2 content.	CO_2 exceptionally high for plate Al. Higher for μm-Al as measured via 358 nm.
Excitation/ electron temperature	With Ar	20–50k K at 100 ns to <10k K at 700 ns to 1 μs as measured via Boltzmann fitting	No clear trend among gas compositions. Higher for single-component gases.	Similar for both samples (within expected errors).
Shock velocity	With Ar	Decreasing (monotonically)	No clear trend among gas compositions.	Powder samples higher than plate.
	Without Ar	Decreasing (monotonically)	Trends monotonically with speed of sound.	Powder samples higher than plate.

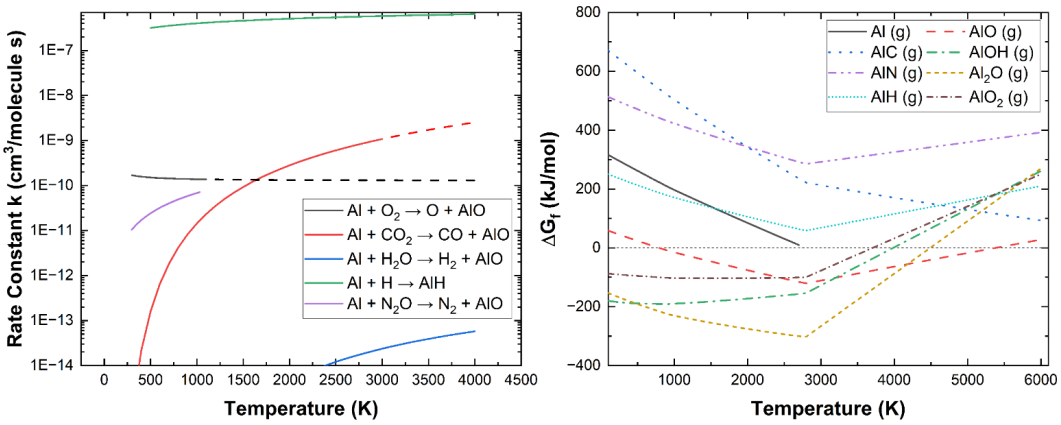

Fig. 19 Kinetic rate constant parameters and Gibbs-free energy of formation for various relevant reactant species with Al as a function of gas temperature, as pulled from the NIST Kinetic Database. Dotted portions of the kinetic rate constant traces are extrapolations from the highest reported temperature from a given source.

The relative effects of molecule disassociation, relative ionization energies, and kinetic reaction rates of O, O_2, and CO_2 directly with gas-phase Al, which is effectively instantaneously produced in the laser pulse, all need to be coupled and better understood. The effect of excess species such as C (which was observed as a potential benefit to other reactive species such as Si in previous work[13]) also needs to be established for Al. Other effects such as the ablation efficiency (dependent on atmospheric pressure) and plasma hydrodynamics (e.g., dispersion of gases and particles behind the shock front) may also affect the laser-induced shock velocity. Significant modeling efforts are needed to understand these effects, and the data presented here provide a starting point of relevant plasma properties under these conditions. Although it seems clear that the inclusion of Ar with the post-detonation gases CO_2 and N_2 significantly affected the resulting plasma chemistry, thus making the data less useful for understanding the influence of post-detonation gases on Al reactivity and energy release, the observed trends can help formulate future studies and provide data relevant to models containing Ar (e.g., explosively generated plasmas).

6. Conclusion

In this work, we have taken the first steps to understand the plasma chemistry in surrogate post-detonation environments using a common energetic additive of Al. Micrometer-scale powder and plate are excited under high-energy pulsed laser ablation under a variety of environmental conditions, including N_2, CO_2, air, and combinations therein with and without Ar. A variety of fundamental plasma properties are presented including electron density, plasma temperatures, ionization ratios, and the temporal evolution of species of interest, including Al I, AlO, C I,

CN, etc. The inclusion of Ar with the post-detonation gases CO_2 and N_2 significantly affected the resulting plasma chemistry (thus making the data less straightforward for understanding the influence of post-detonation gases on Al reactivity and energy release). Significant enhancements in electron density, relative spectral peak intensity, ionization ratio, and so on, were observed in the presence of Ar, which in increasing concentrations appears to increase the laser-induced shock velocity, despite being chemically inert and having a higher native speed of sound. The combination of these results implies a complex interplay between the plasma electron properties (temperature, electron density, etc.), hydrodynamics, exothermic recombination reactions, speed of sound of the medium, gas-phase kinetics, thermodynamic driving forces, and confinement. The results for the Ar-containing mixtures provide interesting insights into the effect of chemically nonreactive (e.g., inert) but plasma-active species for a span of gas mixtures. Future work will focus on Ar-less gas environments and more complex mixtures of post-detonation gases—for example, O, H, CO_2, and N_2.

7. References

1. Cristoretti G, De Giacomo A, Dell'Aglio M, Legnaioli S, Tognoni E, Palleschi V, Omenetto N. Local thermodynamic equilibrium in laser-induced breakdown spectroscopy: beyond the McWhirter criterion. Spectrochim Acta Part B. 2010;65:86–95.
2. Phillips MC, Kautz EJ, Harilal SS. Comparison of excitation and kinetic temperatures in a laser-produced plasma using absorption spectroscopy. Opt Lett. 2023;48:1942–1945.
3. Wen S-B, Mao X, Greif R, Russo RE. Expansion of the laser ablation vapor plume into a background gas. I Anal J Appl Phys. 2007;101:023114.
4. Edwards DH, Lawrence TR, Gaydon AG. Ionization measurements in detonation waves. Proc Royal Soc A. 1965;286:415–439.
5. Zel'dovich YB, Raizer YP. Physics of shock waves and high-temperature hydrodynamic phenomena. Annotated ed. Dover Publications; 2002.
6. Harlin J, Nemzek R. Physical properties of conventional explosives deduced from radio frequency emissions. Propellants Explos Pyrotech. 2009;34:544–550.
7. Kautz EJ, Phillips MC, Zelenyuk A, Harilal SS. Oxidation in laser-generated metal plumes. Phys Plasmas. 2022;29:053509.
8. Polek M, Kautz EJ, Harilal SS, Beg FN. Investigation of nanosecond laser ablation from metal targets. 2022 IEEE International Conference on Plasma Science (ICOPS); 2022. p. 1.
9. Kautz EJ, Phillips MC, Zelenyuk A, Harilal SS. Evolutionary history of atoms and molecules in reactive laser-produced plasmas. 2022 IEEE International Conference on Plasma Science (ICOPS); 2022. p. 1.
10. Kautz EJ, Zelenyuk A, Gwalani B, Phillips MC, Harilal SS. Gas-phase oxidation and nanoparticle formation in multi-element laser ablation plumes. Phys Chem Chem Phys. 2022; 24:26583–26590.
11. Kautz EJ, Zelenyuk A, Gwalani B, Harilal SS. Gas-phase molecular formation in multi-component laser-produced plasmas. 2021 IEEE International Conference on Plasma Science (ICOPS); 2021. p. 1.
12. Gottfried JL, Bukowski EJ. Laser-shocked energetic materials with metal additives: evaluation of chemistry and detonation performance. Appl Opt. 2017: 56:B47–B57.

13. Wainwright ER, Miller CJ, Giri L, Pesce-Rodriguez RA, Wu C-C, Gottfried JL. Influence of silicon particle morphology on laser-induced plasma properties. Spectrochim Acta Part B. 2023;199:106597.

14. Miller CJ, Wainwright ER, Gottfried JL, Abraham J, Wei L, Pantoya ML. The influence of particle size on the fluid dynamics of a laser-induced plasma. Phys Fluids. 2022;34:053312.

15. Wainwright ER, De Lucia FC Jr, Weihs TP, Gottfried JL. Spatiotemporal and emission characteristics of laser-induced plasmas from aluminum-zirconium composite powders. Spectrochim. Acta Part B. 2021;183:106270.

16. Wainwright ER, Dean SW, De Lucia FC Jr, Weihs TP, Gottfried JL. Effect of sample morphology on the spectral and spatiotemporal characteristics of laser-induced plasmas from aluminum. Appl Phys A. 2020;126:83.

17. Buday J, Pořízka P, Buchtová M, Kaiser J. Determination of initial expansion energy with shadowgraphy in laser-induced breakdown spectroscopy. Spectrochim Acta Part B. 2021;182:106254.

18. Calver TI, Shattan MB, Perram GP. Shock front detachment during pulsed laser ablation of graphite. Appl Phys A. 2021;128:15.

19. Wei T, Hargather MJ. A new blast wave scaling. Shock Waves. 2021;31:231–238.

20. Díaz JS, Rigby SE. Blast wave kinematics: theory, experiments, and applications. Shock Waves. 2022;32:405–415.

21. Gottfried JL, Wainwright ER. Laser-induced air shock from energetic materials (LASEM): a novel microscale technique for characterizing energy release at high heating rates. J Energ Mater. 2023. https://doi.org/10.1080/07370652.2023.2200442.

22. Dreizin EL. Metal-based reactive nanomaterials. Prog Energy Combust Sci. 2009;35:141–167.

23. Sarou-Kanian V, Rifflet JC, Millot F, Gökalp I. Aluminum combustion in wet and dry CO_2: consequences for surface reactions. Combust Flame. 2006;145:220–230.

24. Servaites J, Krier H, Melcher JC, Burton RL. Ignition and combustion of aluminum particles in shocked $H_2O/O_2/Ar$ and $CO_2/O_2/Ar$ mixtures. Combust Flame. 2001;125:1040–1054.

25. Braconnier A, Gallier S, Halter F, Chauveau C. Aluminum combustion in CO_2-CO-N_2 mixtures. Proceedings of the Combustion Institute. 2021;38:4355–4363.

26. Xiaoya C, Chen D, Chu Q. Anisotropic combustion of aluminum nanoparticles in carbon dioxide and water flows. J Therm Sci. 2022;31:867–881.

27. Glumac N, Krier H, Bazyn TIM, Eyer R. Temperature measurements of aluminum particles burning in carbon dioxide. Combust Sci Technol. 2005;177:485–511.

28. Bazyn T, Krier H, Glumac N. Combustion of nanoaluminum at elevated pressure and temperature behind reflected shock waves. Combust Flame. 2006;145:703–713.

29. Rossi S, Dreizin EL, Law CK. Combustion of aluminum particles in carbon dioxide. Combust Sci Tech. 2001;164:209–237.

30. King MK. Modeling of single particle aluminum combustion in CO_2–N_2 atmospheres. Int Combust Symp. 1979;17:1317–1328.

31. Piehler TN, De Lucia FC Jr, Munson CA, Homan BE, Miziolek AW, McNesby KL. Temporal evolution of the laser-induced breakdown spectroscopy spectrum of aluminum metal in different bath gases. Appl Opt. 2005; 44:3654–3660.

32. Dawood MS, Margot J. Effect of ambient gas pressure and nature on the temporal evolution of aluminum laser-induced plasmas. AIP Advances. 2014;4.

33. Rezaei F, Karimi P, Tavassoli SH. Estimation of self-absorption effect on aluminum emission in the presence of different noble gases: comparison between thin and thick plasma emission. Appl Opt. 2013;52:5088–5096.

34. Aguilera JA, Aragón C. A comparison of the temperatures and electron densities of laser-produced plasmas obtained in air, argon, and helium at atmospheric pressure. Appl Phys A. 1999;69:S475–S478.

35. Kimblin C, Trainham R, Capelle GA, Mao X, Russo RE. Characterization of laser-induced plasmas as a complement to high-explosive large-scale detonations. AIP Adv. 2017;7:095208.

36. Kwapis EH, Posey JW, Medici E, Berg K, Houim RW, Hartig KC. Experimental and computational investigation into the hydrodynamics and chemical dynamics of laser ablation aluminum plasmas. Phys Chem Chem Phys. 2023;25:15666–15675.

37. Kautz EJ, Zelenyuk A, Gwalani B, Olszta MJ, Phillips MC, Manard MJ, Kimblin CW, Harilal SS. Impact of environmental oxygen on nanoparticle formation and agglomeration in aluminum laser ablation plumes. J Chem Phys. 2023;159:174303.

38. Iida Y. Atomic emission characteristics of laser-induced plasmas in an argon atmosphere at reduced pressure. Applied Spectroscopy. 1989;43:229–234.

39. Ma QL, Motto-Ros V, Lei WQ, Boueri M, Bai XS, Zheng LJ, Zeng HP, Yu J. Temporal and spatial dynamics of laser-induced aluminum plasma in argon background at atmospheric pressure: interplay with the ambient gas. Spectrochim Acta Part B. 2010;65:896–907.

40. Kautz EJ, Senor DJ, Harilal SS. The interplay between laser focusing conditions, expansion dynamics, ablation mechanisms, and emission intensity in ultrafast laser-produced plasmas. J Appl Phys. 2021;130:204901.

41. Gottfried JL. Influence of exothermic chemical reactions on laser-induced shock waves. Phys Chem Chem Phys. 2014;16:21452–21466.

42. Settles GS, Hargather MJ. A review of recent developments in schlieren and shadowgraph techniques. Measurement Sci Technol. 2017;28:042001.

43. Gottfried JL, Wainwright ER, Huang S, Jiang Y, Zheng X. Probing boron thermite energy release at rapid heating rates. J Combust Flame. 2021;231:111491.

44. Wainwright ER, Gottfried JL. Monochromatic laser-induced shockwave measurements with improved data processing for reactive materials. DEVCOM Army Research Laboratory (US); 2021. Report No.: ARL-TR-9211.

45. Ratynskaia S, Dilecce G, Tolias P. Nitrogen optical emission during nanosecond laser ablation of metals: prompt electrons or photo-ionization? 2014;117:409–413.

46. Harilal SS, Skrodzki PJ, Miloshevsky A, Brumfield BE, Phillips MC, Miloshevsky G. On- and off-axis spectral emission features from laser-produced gas breakdown plasmas. Phys Plasma. 2017;24.

47. Chase JMW, Davies CA, Downey JJR, Frurip DJ, McDonald RA, Syverud AN. NIST JANNAF thermochemical tables. NIST Standard Reference Database 13. National Institute of Standards and Technology; 1985.

48. Palleschi V. Avoiding misunderstanding self-absorption in laser-induced breakdown spectroscopy (LIBS) analysis. Spectroscopy. 2022;37:60–62.

49. Kuzuya M, Matsumoto H, Takechi H, Mikami O. Effect of laser energy and atmosphere on the emission characteristics of laser-induced plasmas. Appl Spectrosc. 1993;47:1659–1664.

50. Konjević N, Wiese WL. Experimental Stark widths and shifts for spectral lines of neutral and ionized atoms. 1990;19:1307–1385.

51. Griem HR. Spectral line broadening by plasmas. Academic; 1974.

52. Trunov MA, Schoenitz M, Dreizin EL. Ignition of aluminum powders under different experimental conditions. Propell Explos Pyrotech. 2005;30:36–43.

53. De Lucia FC Jr, Dean SW, Gottfried JL. Commercial aluminum powders, part II: energy release rates induced by rapid heating via pulsed laser excitation. Powder Technol. 2022;399:117161.

54. Lazic V, Palucci A, Jovicevic S, Poggi C, Buono E. Analysis of explosive and other organic residues by laser induced breakdown spectroscopy. Spectrochim Acta Part B. 2009;64:1028–1039.

55. Mansour SAM. Self-absorption effects on electron temperature-measurements utilizing laser induced breakdown spectroscopy (LIBS)-techniques. Opt Photon J. 2015;5:79–90.

56. Aguilera JA, Aragon C. Multi-element Saha-Boltzmann and Boltzmann plots in laser-induced plasmas. Spectrochim Acta Part B. 2007;62:378–385.

57. Kramida AE, Ralchenko Y, Reader J, Team NA. NIST atomic spectra database (version 5.8). National Institute of Standards and Technology; 2020.

58. Bousquet B, Gardette V, Ros VM, Gaudiuso R, Dell'Aglio M, De Giacomo A. Plasma excitation temperature obtained with Boltzmann plot method: significance, precision, trueness and accuracy. Spectrochim Acta Part B. 2023;204:106686.

59. El Sherbini AM, El Sherbini TM, Hegazy H, Cristoforetti G, Legnaioli S, Palleschi V, Pardini L, Salvetti A, Tognoni E. Evaluation of self-absorption coefficients of aluminum emission lines in laser-induced breakdown spectroscopy measurements. Spectrochim Acta Part B. 2005;60:1573–1579.

60. Manion JA, Huie RE, Levin RD, DRB Jr, Orkin WTVL, McGivern WS, Hudgens JW, Knyazev VD, Atkinson DB, Chai E, et al. NIST chemical kinetics database. NIST Standard Reference Database 17. National Institute of Standards and Technology; 2015.

61. Saba M, Kato T, Oguchi T. Chemical kinetics modeling for combustion of Al in CO_2. Combust Flame. 2021; 233:111613.

62. Garland NL. Kinetic studies of boron and aluminum species. In: Fontijn A, editor. Gas Phase Metal Reactions. Elsevier; 1992. p. 73–91.

63. Swihart MT, Catoire L, Legrand B, Gökalp I, Paillard C. Rate constants for the homogeneous gas-phase Al/HCl combustion chemistry. Combust Flame. 2003;132:91–101.

64. Sharipov A, Titova N, Starik A. Kinetics of Al + H_2O reaction: theoretical study. J Phys Chem A. 2011;115:4476–4481.

65. Glumac N. Aluminum nitride emission from a laser-induced plasma in a dispersed aerosol. J Appl Phys. 2005;98.

66. Thareja RK, Sharma AK. Formation of AlN in laser ablated plasma of Al in nitrogen ambient. Phys Stat Sol C. 2005;2:2079–2082.

List of Symbols, Abbreviations, and Acronyms

1-D	one-dimensional
Al	aluminum
AlO	aluminum oxide
Ar	argon
ARL	Army Research Laboratory
CI	confidence interval
CN	carbon nitride
CO_2	carbon dioxide
DEVCOM	US Army Combat Capabilities Development Command
H_2O	water
HE	high explosive
HEPA	high-efficiency particulate air
HMX	1,3,5,7-tetranitro-1,3,5,7-tetrazocane
ICCD	intensified charge-coupled device
IR	infrared
LASEM	laser-induced air shock from energetic materials
LIBS	laser-induced breakdown spectroscopy
LTE	local thermodynamic equilibrium
N_2	nitrogen
NIST	National Institute of Standards and Technology
RDX	1,3,5-trinitro-1,3,5-triazinane
SNR	signal-to-noise ratio
TNT	trinitrotoluene
UHP	ultra-high purity
UV/vis	ultraviolet and visible
v_s	speed of sound

1 (PDF)	DEFENSE TECHNICAL INFORMATION CTR DTIC OCA
1 (PDF)	DEVCOM ARL FCDD RLB CI TECH LIB
1 (PDF)	DEVCOM ARL FCDD RLA WA ER WAINWRIGHT JL GOTTFRIED